

DELFT UNIVERSITY OF TECHNOLOGY

REPORT 20-07

ANALYSIS OF THE AERODYNAMICS IN THE HEATING SECTION OF AN  
ANODE BAKING FURNACE USING NON-LINEAR FINITE ELEMENT  
SIMULATIONS

P.A. NAKATE, D.J.P. LAHAYE, C. VUIK, M. TALICE

Reports of the Delft Institute of Applied Mathematics

Delft 2020

Copyright © 2020 by Delft Institute of Applied Mathematics, Delft, The Netherlands.

No part of the Journal may be reproduced, stored in a retrieval system, or transmitted, in any form or by any means, electronic, mechanical, photocopying, recording, or otherwise, without the prior written permission from Delft Institute of Applied Mathematics, Delft University of Technology, The Netherlands.

Article

# Analysis of the Aerodynamics in the Heating Section of an Anode Baking Furnace using Non-Linear Finite Element Simulations

Prajakta Nakate <sup>1,2</sup> , Domenico Lahaye <sup>1</sup>, Cornelis Vuik <sup>1</sup>, and Marco Talice <sup>3</sup>,

<sup>1</sup> Delft University of Technology; P.A.Nakate@tudelft.nl; D.J.P.Lahaye@tudelft.nl; C.Vuik@tudelft.nl

<sup>2</sup> Aluminium and Chemie, Rotterdam B.V.

<sup>3</sup> PM2ENGINEERING, Cagliari, Italy;

Version December 9, 2020 submitted to Fluids

**Abstract:** The emissions from the industrial furnaces impact the environment. Among the various factories, those having anode baking furnaces are working on reducing the pollutant emissions. The aerodynamics in the furnace influences the emissions due to the high dependence of combustion and radiation phenomena on the mixing characteristics. Therefore, this paper aims to establish the numerical simulation results for the three-dimensional turbulent flow in a single section of an anode baking furnace with a high rate of fuel injection. The stabilized non-linear finite element approach on the RANS equation is used with COMSOL Multiphysics. The turbulent viscosity ratio is highly sensitive to the mesh for the standard  $k-\epsilon$  model. The requirements of the Cartesian and refined mesh near the jet development region is explained. The comparison of meshes generated by two meshing tools namely cfMesh and COMSOL Multiphysics default Mesher is carried out. The high numerical diffusion in the flow models due to the coarser mesh leads to convergence but deficit the precision in the results. This paper shows that the mesh generated by cfMesh with flow aligned refinement combined with the non-linear finite element solver in COMSOL Multiphysics proves to provide accurate results of turbulent quantities.

**Keywords:** Turbulent flow; Industrial furnace; Cartesian mesh; Numerical diffusion

## 1. Introduction

The combustion process is the most important process to extract energy from fossil fuels. The majority of the usage of burning fossil fuels is carried out in industries [1]. The combustion of gaseous hydrocarbon fuels in industries that manufacture raw materials such as steel, glass, cement, etc. is still indispensable due to high energy density levels. The byproduct of the combustion of fossil fuels is the pollutant gases that have a significant impact on environment. Due to the consequential amount of pollutant formation from industries, the governments provide regulations on the allowed pollutant quantities that can be emitted. There have been several studies that propose techniques to curb pollutant gases at the source [2,3]. This encourages industries to make the combustion process more efficient by reducing the formation of pollutant gases, reducing the usage of fuel, and optimizing energy consumption. The traditional trial and error approach is limited due to the difficulty of handling the high temperature. Moreover, the resource requirements for such trials can be high leading to a longer time needed for the successful attempt. The numerical modeling of the process in such applications can be of advantage to achieve an efficient process.

There are numerous industries that are based on the combustion of fossil fuels as the energy source. Aluminium, for example, is extracted from the Bauxite using the Hall-Héroult process. The Hall-Héroult process is the electrolysis process in which anodes wear out continuously. Thus, the

33 anodes need to be regularly replaced. The carbon anodes used in the extraction process should have  
 34 properties such as high density, conductivity, mechanical strength, and low reactivity in the process.  
 35 The anodes need to be baked before using in the Hall-Héroult to gain these properties. This gives rise  
 36 to an auxiliary industry in which anodes are baked. The anode baking process has gained attention  
 37 due to its high costs and energy demand. Figure 1 shows a schematic representation of a horizontal  
 38 ring anode baking furnace. The furnace consists of the flue and the pits in which raw anodes are  
 39 loaded. As shown in Figure 1, the air flows in the horizontal direction through the flue. The left picture  
 40 from Figure 1 shows the channel through which gas flows from one section to another. The combustion  
 41 process occurs in the flue when the injected fuel reacts with air flowing through the channel. The fuel  
 42 is injected from the top holes. The heat generated during the combustion process is conducted through  
 43 the walls and packing material to the anodes.

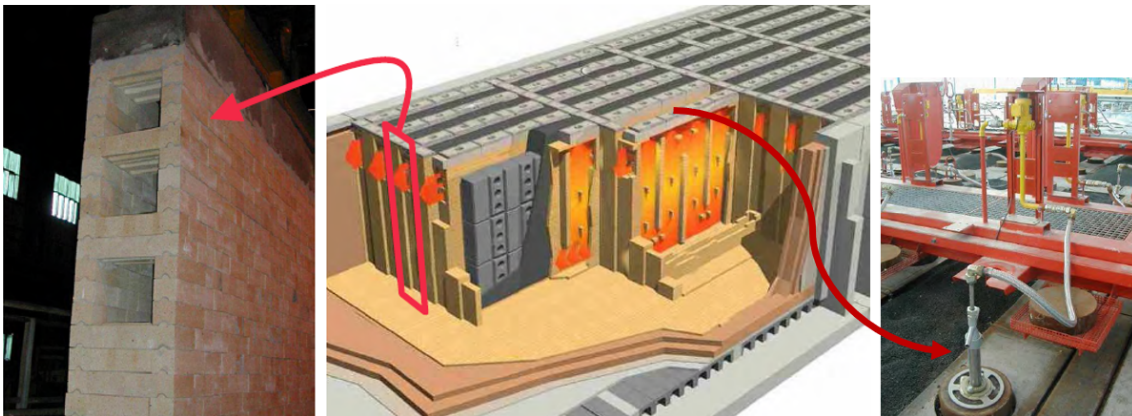


**Figure 1.** The schematic representation of the anode baking furnace. The left-most picture is the photograph from the actual furnace showing the exit of the flue channel. The right-most picture shows a photograph of the burner through which fuel is injected

44 It is important to understand the overall process to define a model. The process in the anode  
 45 baking furnace is such that there is a continuous exchange of heat either from the hot gases to the  
 46 wall or from the walls to the gases. Based on the transfer of heat, the anode baking furnace is divided  
 47 into zones such as preheating, heating, blowing, and cooling zone. Each zone consists of three or  
 48 four sections. Figure 2 presents the schematic representation of the various zones in the anode baking  
 49 furnace. In the preheating zone, the raw anodes are loaded in the pits. Whereas, in the adjacent flue,  
 50 the heated gas exiting from the heating section is circulating. The transfer of heat in this section occurs  
 51 from the flue to the anodes. The temperature of the anodes is increased to approximately 550°C in  
 52 this section. In the heating section, the fuel (natural gas) is injected from the top. Figure 2 shows a  
 53 total of three ramps (one for each section) with two burners on each ramp. In the heating section,  
 54 the combustion of natural gas is carried out due to the contact with air at ignition temperature. The  
 55 transfer of heat occurs from the flue gas to the anodes. As a result, the temperature of anodes further  
 56 increases to approximately 1100°C. In the third zone i.e. blowing zone, the air is injected using the  
 57 blowing ramp. In this zone, the anodes are already heated. Therefore, the transfer of heat occurs  
 58 from the anodes to the cold air. This results in an increase of gas temperature to 1150°C. The last zone  
 59 is the cooling zone in which the anodes are further cooled using external fans so as to post-process.  
 60 Therefore, to study NO<sub>x</sub> emissions, only the heating section of the furnace is important.

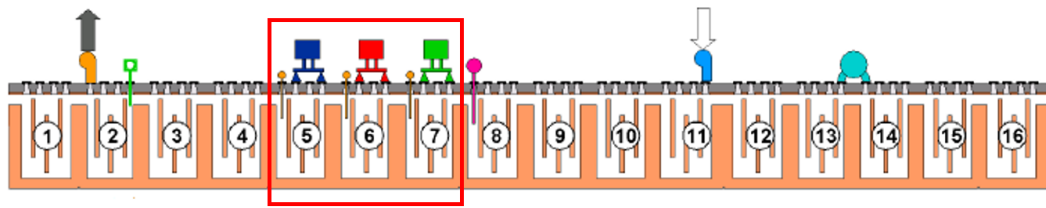


**Figure 2.** The schematic representation of different zones in the anode baking furnace based on the transfer of heat. The sections presented in the red box are in the heating zone. One section (section 7) is studied in this paper due to its importance with respect to the NO<sub>x</sub> generation.

61 The modeling of anode baking furnace has been developed since 1980's [4]. The early models  
 62 form the basis of the anode baking furnace modeling developed further. The literature available on  
 63 the modeling suggests that there is a wider scope of improvement in the anode baking process with  
 64 respect to a variety of goals. Some of the examples are optimizing energy consumption, reducing  
 65 soot and NO<sub>x</sub> formation, increasing the anode quality, and improving the lifespan of the refractory.  
 66 The modeling approach developed by Gosselin et.al. [5] focuses on the choice of combustion model  
 67 for anode baking furnace. They provide the sensitivity of maximum temperature computed by three  
 68 combustion model approaches namely, eddy dissipation model, mixture fraction/pdf model, and hot  
 69 jet approach. The study provides insights on the advantage of the mixture fraction/pdf combustion  
 70 model to predict accurate maximum temperature. The effect of radiation coupling is also essential  
 71 for computing the accurate maximum temperature. The study carried out by Tajik et. al. [6] provides  
 72 results for combinations of turbulent flow models, combustion models, and radiation models. The  
 73 results are extended for the anode baking furnace model. They conclude that the realizable  $k-\epsilon$  model,  
 74 mixture fraction/pdf model, and discrete ordinate-WSGGM (weighted-sum-of-gray-gas-modeling)  
 75 are the appropriate models. Further work by Tajik et. al. [7] on the calculations of NO<sub>x</sub> emissions  
 76 by studying the effect of re-circulation of exhaust gases and diluting the inlet oxygen concentration  
 77 at elevated temperature shows the lowering of emissions. Another modeling by Bessen et. al. [8]  
 78 studies the different parameters of the burner designs for high-velocity fuel injection to predict NO<sub>x</sub>  
 79 formation.

80 Among various industries, Aluchemie BV Rotterdam has anode baking furnaces in The  
 81 Netherlands. Aluchemie is working on reducing the NO<sub>x</sub> emissions from the furnace to meet the  
 82 stringent requirements by local authorities. The furnace geometry of Aluchemie is slightly different  
 83 from the other furnaces presented in the literature. In the models by Gosselin et.al.[5] and by Tajik et.al  
 84 [6], the fuel pipes are inserted deeper into the flue and have a lower fuel injection velocity than is the  
 85 case in this paper. In the Aluchemie furnace, the fuel pipe from the burner does not penetrate directly  
 86 into the furnace. In practice, such penetration in the furnace poses the problem of higher warping of  
 87 fuel pipe. There have been various studies that show the impact of geometry modification on the flow  
 88 dynamics in the furnace [6]. The modeling for the geometry specific to the anode baking furnace of  
 89 Aluchemie is required. Therefore, this work is dedicated to the development of the anode baking  
 90 furnace of Aluchemie. The aerodynamics forms the basis of the modeling in the anode baking process.  
 91 Since no such modeling was carried out in Aluchemie before, the model is developed from scratch.  
 92 Therefore, the model discussed in this paper is based on the Reynolds-averaged Navier-Stokes (RANS)  
 93 equations for modeling the non-reactive turbulent flow. This avoids going over the more complicated  
 94 Large Eddy Simulation (LES) or Direct Numerical Simulation (DNS) models.

95 The goal of this work is to provide suitable modeling techniques to reduce NO<sub>x</sub> emissions from  
 96 the anode baking furnace. It should be noted that NO<sub>x</sub> is not generated in all sections. The temperature  
 97 in the preheating section is not high enough to form NO<sub>x</sub> and therefore, the NO<sub>x</sub> formation in the  
 98 preheating section remains negligible. The temperature in the flue gas in the heating section is more  
 99 than 1300°C and provides suitable conditions for the generation of NO<sub>x</sub>. Therefore, for studying the

100 NOx formation in the anode baking furnace, it is important to focus on the aerodynamics in the heating  
101 sections.

102 In this paper, a detailed analysis of the turbulent flow modeling in a single heating section of the  
103 flue is carried out. The COMSOL Multiphysics software with version 5.4 is used for the modeling. The  
104 COMSOL Multiphysics is a finite element based solver and uses the Newton method with a coupled  
105 pressure-velocity approach [14]. The software has been proven to provide excellent coupling between  
106 different physical phenomena and is easily accessible for academia. With this paper, we aim to provide  
107 converged simulation results of the turbulent flow in the heating section of the anode baking furnace.  
108 Moreover, the role of the Newton solver for coupled pressure-velocity approach on the Cartesian mesh  
109 of realistic geometry is elaborated.

110 The anode baking process is a multi-physical phenomenon. Understanding the aerodynamics  
111 in the furnace is crucial for modeling the NOx formation due to the high dependence of combustion  
112 and radiation on the flow. This motivates us to describe the flow simulation results in detail. The  
113 accuracy of any numerical model depends significantly on the discretization of the equations under  
114 investigation. The finite element discretization used in the current work is further dependent on the  
115 type of mesh. Due to the complexity of anode baking furnace geometry, it is not straightforward to  
116 obtain the desired mesh. Therefore, the analysis of the results with varying meshes is important. In  
117 this work, the results with the two meshing tools namely, cfMesh version 3.2 and COMSOL default  
118 mesher are compared using the standard  $k-\epsilon$  model. Moreover, the sensitivity of the solution to the  
119 refinement in the region of jet development is studied. The effect on the results due to the higher  
120 numerical diffusion of coarser mesh is explained. The study is extended to the less diffusive realizable  
121  $k-\epsilon$  model. The effect of various parameters on the convergence behavior of the realizable  $k-\epsilon$  model  
122 is described to provide guidelines on getting the converged solution. The paper describes the role  
123 of the Cartesian and flow aligned mesh to improve the flow description as well as their effect on the  
124 convergence behavior.

125 In the next section, the geometry definition, non-isothermal cross-flow conditions, mesh  
126 generation techniques, governing equations, finite elements discretization, and the pseudo-time  
127 stepping solver within non-linear and linear equations is described. In the results section, the baseline  
128 model is discussed followed by a comparison with various meshes. In the next section, the challenges  
129 in the convergence of the realizable  $k-\epsilon$  model are discussed.

## 130 2. Model Description

### 131 2.1. Geometry Definition

132 The source of the NOx formation in the anode baking furnace is in the heating sections. In other  
133 sections of the furnace, high-temperature zones required for the formation of NOx are not observed.  
134 Therefore, the model is confined to the heating section of the furnace in this study. The geometry of  
135 the model is as shown in Figure 3. To study the effect of the design parameters, there have various flue  
136 designs modeled in the published literature [6,8]. The geometry of the model studied in this paper is  
137 based on the existing furnace design from Aluchemie factory. The length of the outlet pipe is such  
138 that the backflow is suppressed and uniform pressure distribution is ensured at the outlet. The focus  
139 of the paper is to understand the importance of accurate computation of the flow of the gas in the  
140 furnace. Therefore, the geometry consists of only the flue domain. The geometry consists of three air  
141 inlet pipes, three outlet pipes, and two fuel inlets as shown in Figure 3. The burner has been simplified  
142 to a simple pipe with a length of 1.1 m and a diameter of 0.009 m. The typical bypass dimensions at  
143 top and bottom are 0.084 [m] in y-direction. The rectangular obstacles with smoothed corners are the  
144 tie-bricks required for the structural strength of the furnace and also aids in providing turbulence. The  
145 three baffles direct the flow in the desired direction. The symmetry in the flue wall is assumed. The  
146 geometry files are available for download in different formats such as IGES and STEP so as to provide  
147 open-domain benchmark configuration.

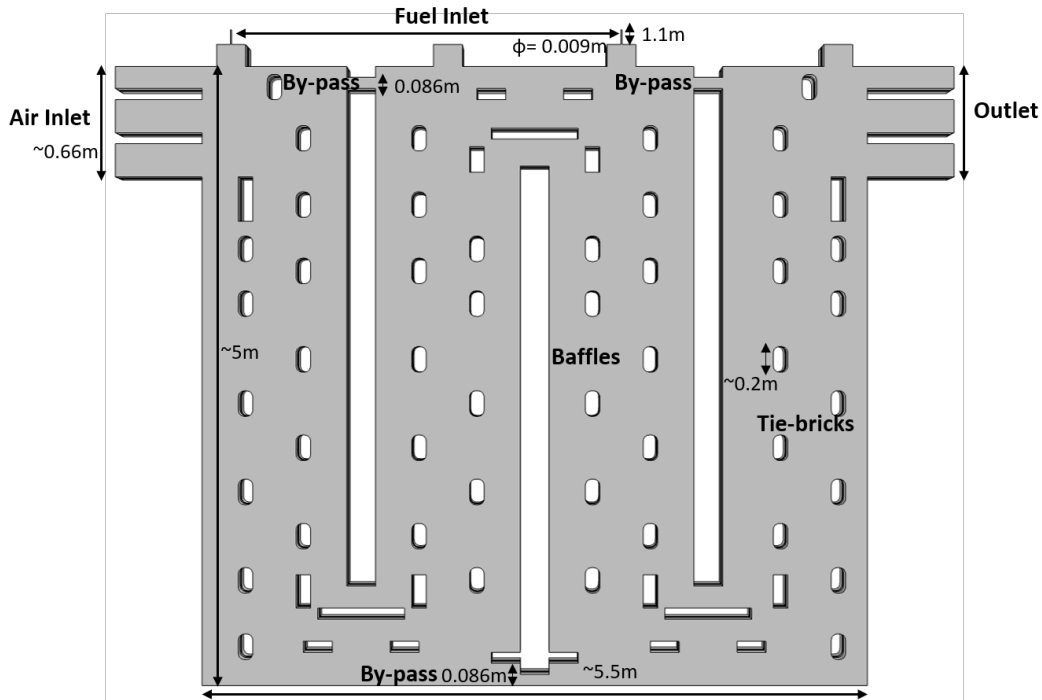


**Figure 3.** The geometry of the heating section of the anode baking furnace model

## 148 2.2. Non-isothermal Fuel Jets in Cross-Flow

149 The overall anode baking furnace modeling consists of various phases namely a gas phase on the  
 150 flue side and a solid phase on the wall, anodes, and packing coke. In this paper, the focus is only on the  
 151 gas phase in the furnace. The flow in the heating section of an anode baking furnace is characterized  
 152 by the air from the side inlets and fuel flow from the top inlets. The outlet is on the other side in the  
 153 perpendicular direction to the fuel inlet as shown in Figure 3. The air and fuel interact in a cross-flow  
 154 manner. Apart from providing structural strength, the tie-bricks also aids in the aerodynamics of  
 155 the flow. The small openings at the top of the furnace are required to avoid the dead flow and the  
 156 associated hot spots at the corners. The presence of baffles directs the flow in the U shape providing  
 157 maximum mixing of the air and the fuel and assure overall heating of the wall. Aluchemie furnaces  
 158 have by-passes to avoid hot spots in the dead zones and thereby, ensuring safety in the furnace.

159 The Reynolds number at the fuel inlet and air inlet are around 13000 and 8500, respectively. Table  
 160 1 provides the fuel inlet and air inlet boundary conditions. Due to the high velocity of the fuel, the jet is  
 161 expected to penetrate deeper and provide higher turbulent mixing. The presence of tie-bricks generates  
 162 backflow due to the adverse pressure gradient. The effects of the backflow are highly dependent on  
 163 the velocity of the jet.

**Table 1.** Inflow conditions at fuel and air inlets

Property	Symbol	Air Inlet	Fuel Inlets
Velocity [m/s]	$U_{ref}$	1.45	74
Temperature [K]	T	1050	300
Re [-]	Re	8500	13000
Turbulent length scale [m]	$L_T$	0.01	0.01
Turbulent intensity [%]	$I_T$	0.05	0.05

164 The air and fuel streams are injected at different temperatures. The effect of temperature variations  
 165 on the flow is considered by taking into account the variation of density with respect to the temperature.  
 166 The physical properties of the gas in the flue are as mentioned in Table 2.

**Table 2.** Physical properties of the gas

Physical property	Symbol	Values
Specific heat capacity [J/(kg*K)]	$C_p$	1004.5
Ratio of specific heats [-]	$\gamma$	1.4
Prandtl number [-]	$Pr$	0.73
Molecular viscosity [kg/(m*s)]	$\mu$	$1.8 \cdot 10^{-5}$

### 167 2.3. Mesh Generation

168 The outcome of the numerical model of flow computations is highly influenced by the mesh.  
 169 The burners used in the Aluchemie operates at high velocity of fuel injection. The computations of  
 170 higher velocity regime demands for the Cartesian and flow aligned mesh . As will be discussed later,  
 171 non-linear finite element solver is utilized in the present study which further requires a better quality  
 172 mesh.

173 The requirement of the Cartesian mesh is elaborated in the previous work [10]. The detailed  
 174 analysis shows that the differences in the results obtained by two simulation environments is due to  
 175 the size and structure of the mesh. The presence of tie-bricks, by passes and baffles impose challenges  
 176 to obtain a hexahedral mesh. The dimensions of the geometrical entities varies from mm to m in  
 177 the flue domain of the anode baking furnace. Moreover, the turbulent flow in the furnace is such  
 178 that a refined mesh is required in the regions of interaction of air and fuel. To generate such mesh  
 179 with the available meshing techniques in COMSOL Multiphysics is difficult. In the results section,  
 180 the inefficacy of the mesh generated with the COMSOL software for the anode baking application is  
 181 described. Therefore, advanced software dedicated for the mesh generation is required. In this study,  
 182 a new meshing technique is developed to construct a well-structured Cartesian mesh with cfMesh  
 183 software version 3.2.1.

184 cfMesh is a collection of mesh generation tools distributed as a library [11]. This library is designed  
 185 to provide customizable meshing workflows for automatic generation of meshes with various cell  
 186 types in complex geometries of industrial interest. cfMesh generates hex-dominant meshes, tetrahedral  
 187 meshes, meshes consisting of arbitrary polyhedra, and 2D quad-dominant meshes. The library uses  
 188 both shared-memory with OpenMP and distributed-memory parallelization with MPI. Parallelisation  
 189 is encapsulated inside the meshing algorithms. Hence, it allows customization of meshing process  
 190 while preserving the benefits of the code executing in parallel.

191 The meshing process is controlled by a geometry file given as a surface triangulation, most often  
 192 as an STL file, and a dictionary containing the parameters provided by the user. Once the geometry  
 193 and the settings are given, the mesher generates the mesh automatically without any user intervention.  
 194 The dictionary allows the user to specify the global cell size in the domain and local refinement zones.  
 195 The latter can be specified via subsets, surface meshes, edges mesh, as well as via objects such as  
 196 cylinders, boxes, spheres and lines. The dictionary also allows to control the number of boundary  
 197 layers at each boundary of the domain, their number and their thickness ratio. Dictionary settings  
 198 allow mesh-sensitivity studies by changing a single parameter. The algorithms used by cfMesh are  
 199 described in [11]. A workflow is developed to generate mesh and convert it into a suitable format  
 200 for importing into COMSOL® Multiphysics. The output of the cfMesh is in the format supported by  
 201 OpenFOAM whereas COMSOL® Multiphysics supports importing mesh in Nastran format. Therefore,  
 202 a conversion tool is developed using OpenFOAM utility that converts FOAM mesh into Nastran.  
 203 This conversion tool which is a source code of the OpenFOAM utility is available for download. The  
 204 various meshes studied and compared in this study are summerised in Table 3.

**Table 3.** Different meshes analysed in this study

Label	Mesh generation tool	Characteristics
Mesh 1	cfMesh	Refinement under burner
Mesh 2	COMSOL	Refinement under burner
Mesh 3	cfMesh	No Refinement under burner

205 Figure 4 shows the Mesh 1 of the complete heating section of the anode baking furnace that is  
 206 referred to as the 'Baseline model' in the further sections. As will be discussed later, the model provides  
 207 accurate qualitative results as compared to Mesh 2 and Mesh 3 with the standard  $k-\epsilon$  model.

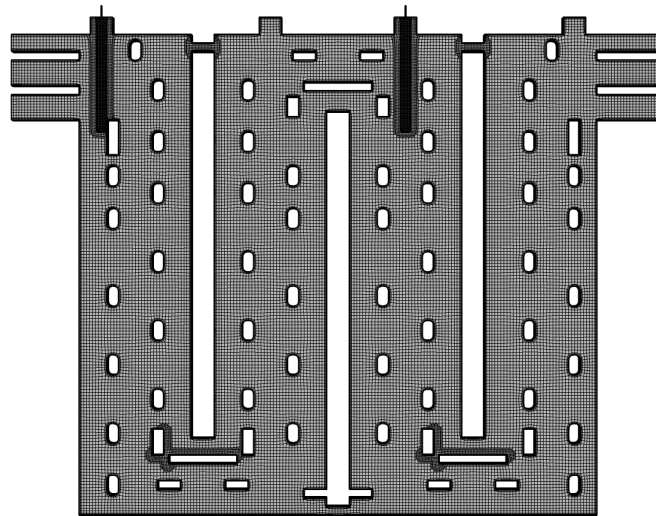


**Figure 4.** The Cartesian mesh generated by the software cfMesh (Mesh 1) of the heating section of the anode baking furnace

208 To analyse the effect of mesh on the turbulent flow dynamics, following mesh comparisons are  
 209 carried out.

- 210 • Mesh obtained by cfMesh (Mesh 1) and COMSOL (Mesh 2)
- 211 • Mesh obtained by cfMesh (Mesh 2) with and without local refinement (Mesh 3)

212 Figure 5 shows the difference between the mesh generated by cfMesh and COMSOL Multiphysics  
 213 software at the symmetry plane near the fuel inlet and at the YZ plane cut through jet region. It can be  
 214 observed that even though with both meshing softwares, the mesh is refined near fuel inlet, the mesh  
 215 generated by cfMesh is Cartesian. Table 5 shows the number of elements and average mesh quality  
 216 based on the skewness parameter. The average mesh quality of 1 is a good mesh. Even with the higher  
 217 number of elements with the COMSOL mesh, the quality of the elements remains low.

**Table 4.** The details of the two meshes with different meshing tools

	cfMesh	COMSOL Mesh
Number of elements	545694	4375821
Average mesh quality	0.861	0.666

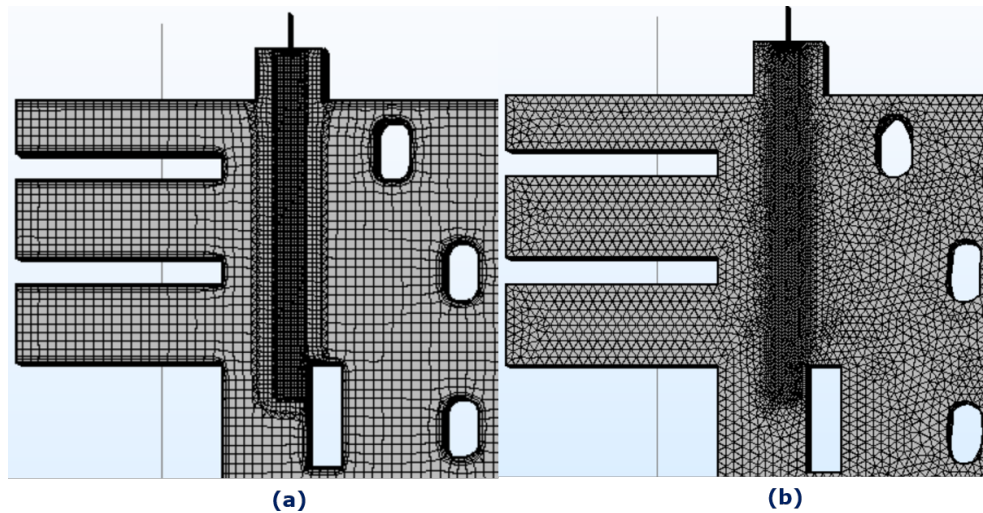


**Figure 5.** Mesh at the symmetry plane in the flue wall prepared in cfMesh (Mesh 1) and COMSOL (Mesh 2) software respectively

218 In the current application, the region of interest lies beneath the fuel outlet. Therefore, the local  
 219 mesh refinement is carried out in the flow regime of fuel injection. The difference between the number  
 220 of elements and the average quality of the mesh with and without such local refinement is provided in  
 221 Table 5. Figure 6 shows the pictorial representation of the jet refinement.

**Table 5.** The details of the two meshes with different meshing tools

	Number of cells	Average mesh quality
Mesh with jet refinement	545694	0.86
Mesh without jet refinement	470048	0.89

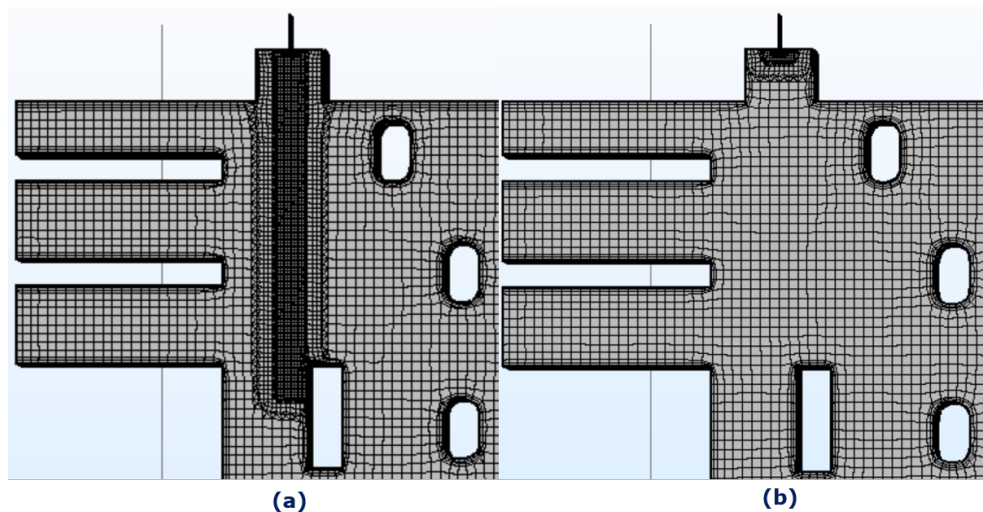


**Figure 6.** Mesh at the symmetry plane in the heating section prepared in cfMesh a) with jet refinement (Mesh 1) and b) without jet refinement (Mesh 3)

222 In all meshes, the boundary layer refinement is introduced. This refinement is important near the  
 223 walls where the no-slip boundary condition is employed. The number of boundary layers, refinement  
 224 of the first layer thickness, and the growth rate of the layers are decided by analyzing the  $y^+$  values.  
 225 These values should be close to 11.06.

## 2.4. Governing Equations

In this paper, the gas flow dynamics in the furnace are discussed. The changes in the temperature of the gas phase of the furnace are low as compared to the solid phase. Therefore, the model can be treated as steady-state. This paper is dedicated to the analysis of turbulent flow calculations. Therefore, all relevant equations are provided in this section.

### 2.4.1. Flow Equation

The gas flow in the furnace is governed by the conservation of mass i.e. continuity equation and the momentum equation given by the Navier-Stokes equation. In the non-isothermal environment, the density variation as a function of temperature has to be considered. The final formulation for the continuity equation for a steady-state flow is presented by the Equation 1. The equation of state is used to compute the density.

$$\nabla \cdot (\rho \mathbf{u}) = 0 \quad (1)$$

The modeling of turbulent flow has been the broad area of research due to their wide application fields. The major obstacle in the modeling of turbulence is the fact that eddies' length scale continuously varies from the largest scale (the same scale of the object) down to the dissipation scale. These eddies have an extensive range in length and time scales and their interactions can be difficult to model. As discussed earlier, the RANS numerical model is used for turbulence modeling. The RANS equation is based on time averaging of the Navier-Stokes equation and accounting for the effect of turbulence on the mean flow. The time-averaging introduces a new term in the equation, Reynolds stresses. These stresses need additional models for the closure. This is carried out by the empirical turbulence models. The Navier-Stokes equation is modified to RANS as per the Equation 2. The Reynolds stress term in the Equation 2 is defined based on the Boussinesq eddy-viscosity assumption.

$$\rho(\mathbf{u} \cdot \nabla) \mathbf{u} = \nabla \cdot [-p\mathbf{I} + \mathbf{K}] \quad (2)$$

Where,

$$\mathbf{K} = (\mu + \mu_t)(\nabla \mathbf{u} + (\nabla \mathbf{u})^T) - \frac{2}{3}(\mu + \mu_t)(\nabla \cdot \mathbf{u})\mathbf{I} - \frac{2}{3}\rho k\mathbf{I} \quad (3)$$

The definition of viscosity term  $\mu_t$  from Equation 3 is dependent on the choice of the turbulent model. The standard  $k$ - $\epsilon$  model and realizable  $k$ - $\epsilon$  model are discussed in this paper.

### 2.4.2. Standard $k$ - $\epsilon$ model

The standard  $k$ - $\epsilon$  model is formulated based on the two transport equations namely for turbulent kinetic energy and the turbulent dissipation rate. Equation 4 and 5 represent the transport equation of turbulent kinetic energy and turbulent dissipation rate, respectively.

$$\rho(\mathbf{u} \cdot \nabla)k = \nabla \cdot \left[ \left( \mu + \frac{\mu_t}{\sigma_k} \right) \nabla k \right] + P_k - \rho\epsilon \quad (4)$$

$$\rho(\mathbf{u} \cdot \nabla)\epsilon = \nabla \cdot \left[ \left( \mu + \frac{\mu_t}{\sigma_\epsilon} \right) \nabla \epsilon \right] + C_{\epsilon 1} \frac{\epsilon}{k} P_k - C_{\epsilon 2} \rho \frac{\epsilon^2}{k} \quad (5)$$

The turbulent viscosity in standard  $k$ - $\epsilon$  model is defined by the Equation 6.

$$\mu_t = \rho C_\mu \frac{k^2}{\epsilon} \quad (6)$$

Where,  $C_\mu$  is constant. The production term in Equation 4 and 5 is defined by the Equation 7.

$$P_k = \mu_t [\nabla \mathbf{u} : (\nabla \mathbf{u} + (\nabla \mathbf{u})^T) - \frac{2}{3}(\nabla \cdot \mathbf{u})^2] - \frac{2}{3}\rho k \nabla \cdot \mathbf{u} \quad (7)$$

### 235 2.4.3. Realizable $k$ - $\epsilon$ model

The formulation of the realizable  $k$ - $\epsilon$  model is similar to the standard  $k$ - $\epsilon$  model. This model also consists of two transport equations for turbulent kinetic energy and turbulent dissipation rate. The turbulent kinetic energy equation is exactly the same as Equation 4. However, the transport equation of the turbulent dissipation rate is improved by accounting for the mean flow distortion. The equation for the turbulent dissipation rate for the realizable  $k$ - $\epsilon$  model is given by Equation 8.

$$\rho(\mathbf{u} \cdot \nabla)\epsilon = \nabla \cdot \left[ \left( \mu + \frac{\mu_t}{\sigma_\epsilon} \right) \nabla \epsilon \right] + C_{1\rho} S \epsilon - C_{\epsilon 2} \frac{\rho \epsilon^2}{k + \sqrt{\nu \epsilon}} \quad (8)$$

The turbulent viscosity in realizable  $k$ - $\epsilon$  model is also defined by the Equation 6. But  $C_\mu$  is not constant and is defined by the series of equation from Equation 9 to 14.

$$C_\mu = \frac{1}{A_0 + A_s U^{(*)} \frac{k}{\epsilon}} \quad (9)$$

$$A_s = \sqrt{6} \cos\left(\frac{1}{3} \arccos(\sqrt{6}W)\right) \quad (10)$$

$$W = \frac{2\sqrt{2}\mathbf{S}_{ij}\mathbf{S}_{jk}\mathbf{S}_{ki}}{\mathbf{S}^3} \quad (11)$$

$$U^{(*)} = \sqrt{\mathbf{S}_{ij}\mathbf{S}_{ij} + \Omega_{ij}\Omega_{ij}} \quad (12)$$

$$\mathbf{S} = \frac{1}{2}(\nabla \mathbf{u} + (\nabla \mathbf{u})^T) \quad (13)$$

$$\Omega = \frac{1}{2}(\nabla \mathbf{u} - (\nabla \mathbf{u})^T) \quad (14)$$

The boundary conditions for both standard and realizable  $k$ - $\epsilon$  model are equally specified. The inlet velocities at air and fuel inlet are defined as Dirichlet boundary conditions. Their values are given in Table 1. The  $k$  and  $\epsilon$  at the inlet of air and fuel are defined based on the reference velocity, turbulent length scale, and turbulent intensity as presented in Equation 15 and 16. The values of these variables are as provided in Table 1.

$$k = \frac{3}{2}(U_{ref} I_T)^2 \quad (15)$$

$$\epsilon = C_\mu^{(3/4)} \frac{k^{(3/2)}}{L_T} \quad (16)$$

The analytical expression known as wall function is used to describe the flow near walls. The domain of computation is considered located at a distance  $\delta_w$  such that the  $\delta_w^+$  computed by Equation 17 is close to 11.06. The  $\delta_w^+$  distance presents the location at which the logarithmic layer meets the viscous sublayer. The value 11.06 is explained in the work of Grotjans and Menter [12]. At this distance both linear relations given in Equation 18 and 19 holds true. The value 11.06 is the optimized solution for these two relations solved at default values of  $\kappa$  and  $\beta$ . The  $\delta_w$  is adjusted such that its value is not less than half of the cell size near the boundary mesh cell.

$$\delta_w^+ = \rho u_\tau \delta_w / \mu \quad (17)$$

$$y^+ = \frac{1}{\kappa} \log y^+ + \beta \quad (18)$$

$$y^+ = \frac{|u|}{u_\tau} \quad (19)$$

236 At the outlet, the pressure boundary condition is specified such that the flow is normal to the outlet  
 237 boundary. The symmetry boundary condition is defined at the middle plane.

#### 238 2.4.4. Energy Equation

An energy equation as presented in Equation 20 is required to solve the non-isothermal flow model.

$$\rho C_p \mathbf{u} \cdot \nabla T + \nabla \cdot \mathbf{q} = Q \quad (20)$$

Where,  $\mathbf{q}$  is computed by Equation 21.

$$\mathbf{q} = -k \nabla T \quad (21)$$

239 The temperature at the inlet of air and fuel is defined as the Dirichlet boundary condition as presented  
 240 in Table 1. The energy flux is in the normal direction at the outlet boundary. The symmetry boundary  
 241 condition similar to the flow equation is defined for the energy equation as well.

#### 242 2.5. Finite Element Discretization

243 In this work, COMSOL® Multiphysics software version 5.4 is used for the simulation. The  
 244 finite element method is used to discretize the underlying partial differential equations. For the  
 245 fluid flow, P1-P1 discretization is applied which means that for both velocity and pressure piecewise  
 246 linear interpolation shape functions are used. COMSOL® Multiphysics applies the Galerkin finite  
 247 element method to solve highly non-linear equations such as the Navier-Stokes equation. These  
 248 equations can become unstable especially if the flow is convection dominated. Therefore, three types of  
 249 stabilizations namely streamline diffusion, crosswind diffusion, and isotropic diffusion are applied. The  
 250 Babuska-Brezzi condition i.e. the requirement of higher-order shape function of velocity than pressure  
 251 is circumvented using the streamline diffusion as described by Hughes et.al. [13]. Streamline diffusion  
 252 also stabilizes the flow when it is dominated by convection. The streamline diffusion formulation in  
 253 COMSOL Multiphysics recovers either streamline upwind Petrov-Galerkin formulation or Galerkin  
 254 least-squares formulation for Navier-Stokes equation. The basic idea behind these formulations is  
 255 the addition of perturbation term in the weighting functions [13]. The streamline diffusion obtains a  
 256 smooth numerical solution if the exact solution is smooth. The solution deviates from the exact solution  
 257 at the boundaries. In order to reduce the spurious oscillations at the boundaries, a weak term is added  
 258 to the transport equation which is termed as crosswind stabilization. In the case of discontinuities  
 259 at sharp gradients, the crosswind diffusion is added orthogonal to the streamline diffusion. In other  
 260 words, crosswind diffusion introduces extra diffusion in boundary layers and shear layers.

261 The maximum Mach number in the furnace is 0.22. Therefore, the flow can be assumed as  
 262 incompressible. In COMSOL Multiphysics software, the incompressible module assumes the density  
 263 to be constant whereas the compressible module for Mach number less than 0.3 can take into account  
 264 the density variation with temperature. In this work, the density is the function of temperature.  
 265 Therefore, the compressible module with Mach number less than 0.3 has been used.

266 The realizable  $k$ - $\epsilon$  model is less diffusive and is not as robust as the standard  $k$ - $\epsilon$  model. Therefore,  
 267 the mesh suitable for the realizable  $k$ - $\epsilon$  model needs further analysis. The shape functions used for  
 268 turbulent quantities and temperature are linear as well. The streamline and crosswind diffusion  
 269 described above are also added to the turbulent model equations.

#### 270 2.6. Pseudo-time stepping solver with non-linear and linear equations

The overall flowchart of the solver settings is represented in Figure 7. As described in the previous section of the numerical model, the non-isothermal turbulent flow consists of a system of equations that includes Navier-Stokes (RANS), turbulent transport equation, and the heat equation. In order to avoid the ill-conditioning of the system, a segregated approach is adapted. The system of equations is distributed in three segregated steps, first for velocity and pressure, second for turbulent quantities, and third for temperature. A damped Newton method with a constant damping factor is used to

linearize the non-linear equation. To drive the convergence towards steady-state while using constant damping factor, COMSOL provides a stabilization method called pseudo-time stepping. In this method, a pseudo time step  $\tilde{\Delta t}$  is introduced as shown in Equation 22. The *nojac* function in COMSOL excludes the expression under operation from the Jacobian computation. The first term from Equation 22 is always zero and does not affect the solution. However, it helps to convert the non-linear iteration into a step size of  $\tilde{\Delta t}$ . The step size is related to the local CFL number which is controlled by the PID controller. This method speeds up the convergence of the model towards a steady state.

$$\rho \frac{\mathbf{u} - \text{nojac}(\mathbf{u})}{\tilde{\Delta t}} + \rho(\mathbf{u} \cdot \nabla)\mathbf{u} = \nabla \cdot [-p\mathbf{I} + \mu(\nabla\mathbf{u} + (\nabla\mathbf{u})^T)] \quad (22)$$

271 To balance the highly non-linear source terms of turbulence transport equations three iterations of  
 272 turbulent transport equation are carried out before proceeding to the next Navier-Stokes iteration.  
 273 The linearized equation in each group is solved using the GMRES iterative solver due to their lower  
 274 requirement of memory with Smoothed Aggregated Algebraic Multigrid (SAAMG) as a preconditioner.  
 275 The SOR line are used as smoothers. A coarser mesh is prepared algebraically in SAAMG as opposed  
 276 to the Geometric Multigrid (GMG) approach in which actual additional meshes are required. Since the  
 277 external meshes are imported into COMSOL® Multiphysics software, additional meshes for GMG  
 278 have to be provided externally as well. Therefore, though GMG is computationally faster, SAAMG is a  
 279 better choice for the current study. Five Multigrid levels with coarse level matrices prepared using the  
 280 Galerkin projection method are used. The V-cycle algorithm is implemented for each multigrid cycle.  
 281 The MUMPS direct solver is used on the coarsest level [15].

### 282 3. Results and Discussion

283 In this section, results of the flow modeling in the heating section of an anode baking furnace are  
 284 discussed. In the first part of the section, the results of the 'Baseline model' with Mesh 1 are presented.  
 285 Further, the non-isothermal results with the standard  $k-\epsilon$  model are compared for two meshing types  
 286 namely with cfMesh (Mesh 1) and COMSOL default mesher (Mesh 2). The NO<sub>x</sub> formation is typically  
 287 in the region of jet development which is a region of interest for this work. Therefore, the sensitivity of  
 288 refinement in the region of jet development is studied by comparing Mesh 1 and Mesh 3. The study is  
 289 extended for the realizable  $k-\epsilon$  model which is less diffusive as compared to the standard  $k-\epsilon$  model.  
 290 The convergence of the realizable  $k-\epsilon$  model is difficult to achieve. The effect of the mesh structure in  
 291 the jet, stabilization techniques, accuracy of the linear solvers, and pseudo time stepping parameters  
 292 on the convergence behavior of the realizable  $k-\epsilon$  model are discussed.

#### 293 3.1. Baseline model with Mesh 1

294 The models are systematically developed by solving isothermal airflow (step 1) at the first instance.  
 295 The solution is used as the initial condition for the model in which fuel is added starting from low to  
 296 high velocity (step 2). The isothermal model is used as an initial guess for the further non-isothermal  
 297 flow model (step 3). As a next step, the artificial stabilization parameter is removed (step 4) to improve  
 298 the accuracy of the results. The Intel(R) Xeon(R) Gold 6152 CPU with 22 cores is used to simulate the  
 299 models. The approximate CPU time required for the simulations of the standard  $k-\epsilon$  model is provided  
 300 in Table 6. To summarize, each line from Table 6 generates the initial guess for the next line.

**Table 6.** CPU time required for the simulation steps for baseline model with Mesh 1

Simulation step	CPU time	Newton iterations	GMRES iterations (v,p)	GMRES iterations (k, $\epsilon$ )
step 1	1 hour 35 mins	22	478	1674
step 2	2 hours 11 mins	25	479	1812
step 3	1 hour 6 mins	48	222	710
step 4	2 hours 33 mins	121	1027	699

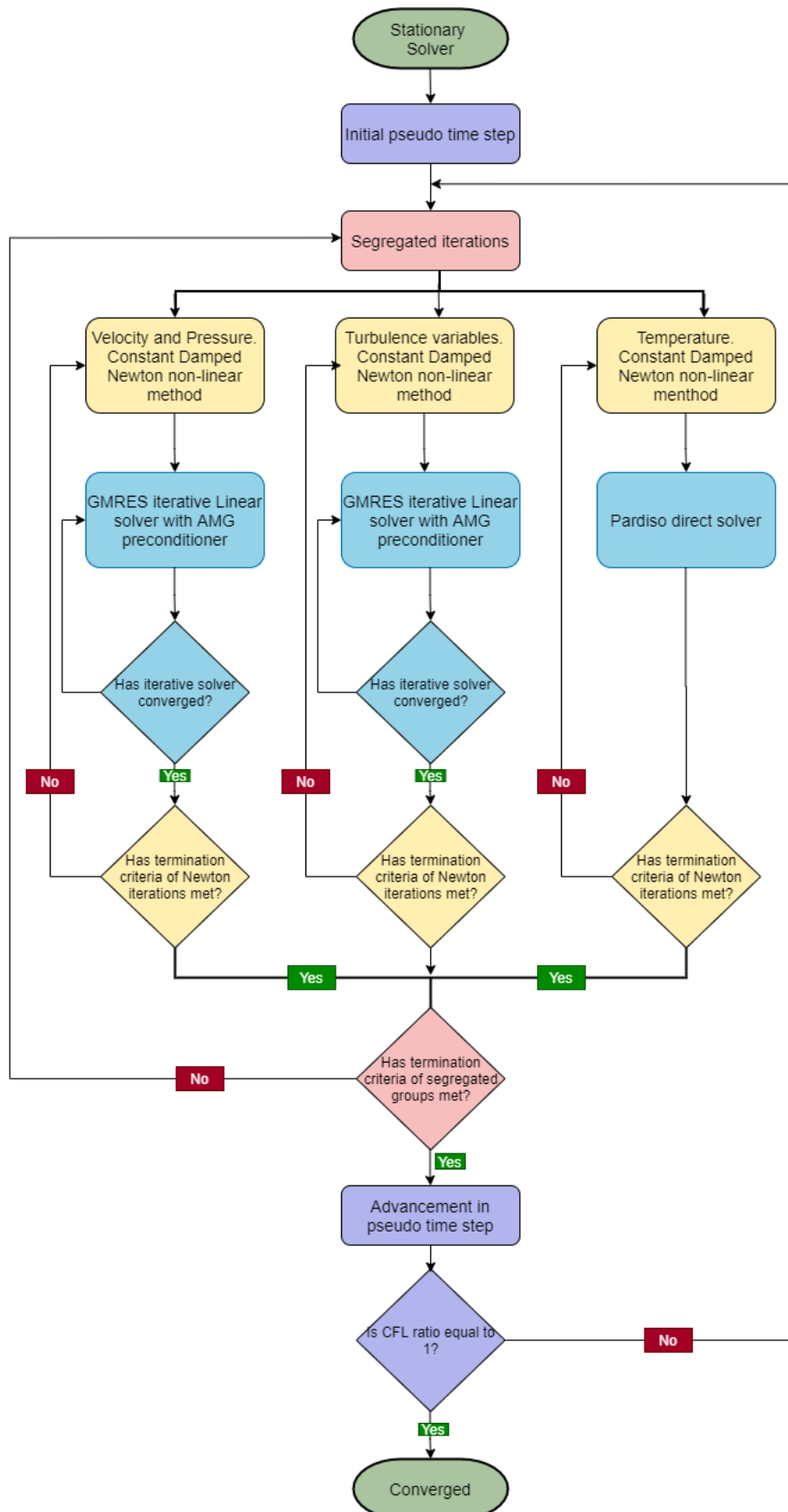


**Figure 7.** The flowchart of non-isothermal non-linear flow solver in COMSOL Multiphysics

301 The non-isothermal results of the baseline model with Mesh 1 are presented in Figure 8. The  $y^+$   
 302 values for the model range from 11.1 to 287. However, the  $y^+$  values are close to 11.06 in most of the  
 303 region. The baseline model is decided on the basis of the qualitative behaviour of the solution. The  
 304 solution of this model for velocity, turbulent viscosity ratio, and temperature are as shown in Figure 8  
 305 (a), (b) and (c) respectively, aligns with the expected physical behaviour. The baseline model serves as  
 306 the reference for the analysis of the other meshes studied in this paper.

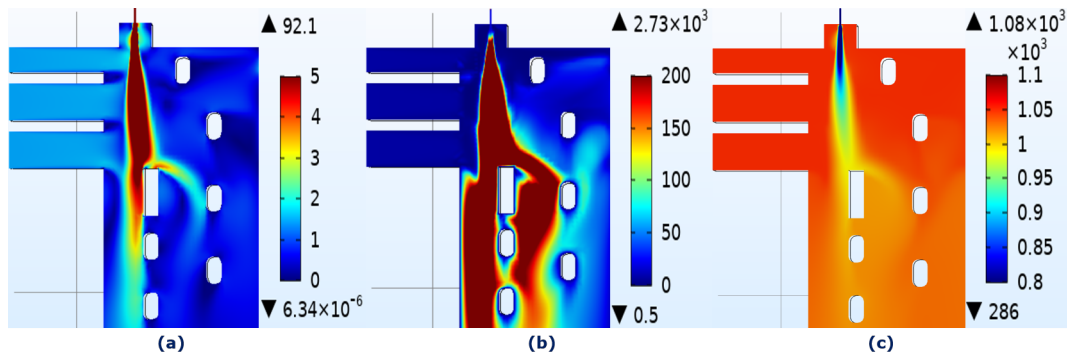


**Figure 8.** The color plots of (a) velocity (b) turbulent viscosity ratio and (c) temperature at the symmetry plane of baseline model with Mesh 1

307 As discussed in Figure 7, the non-isothermal model is solved by segregating physics into different  
 308 groups. The convergence behaviour of the three segregated groups is as shown in Figure 9. The  
 309 stopping criteria for the solver is set at relative tolerance of  $10^{-3}$  which is sufficient for the current  
 310 application. The solver is converged if relative tolerance exceeds the relative error.

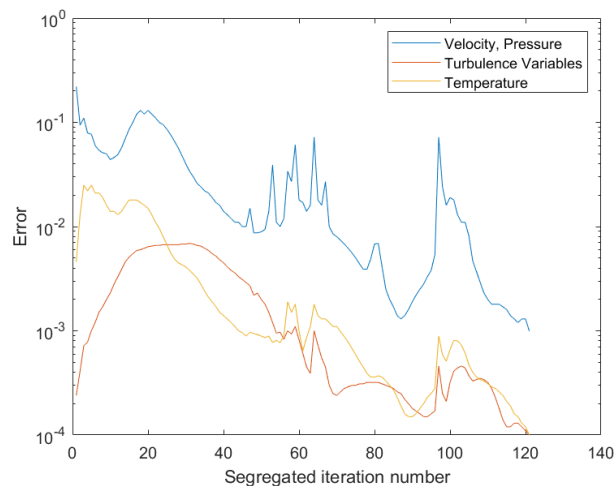


**Figure 9.** The convergence plot for the three segregated groups of different physics for baseline model with Mesh 1. The convergence is plotted for the step 4 from Table 6

### 311 3.2. Non-isothermal effect on baseline model with Mesh 1

312 The non-isothermal effect on the velocity and the turbulent viscosity ratio is shown in Figure 10.  
 313 Due to the varying density, the jet is penetrating further into the furnace. The temperature coupling  
 314 steadily increases the temperature of the jet reducing the density. This results in the deeper penetration  
 315 of the jet. The effect of obstacles by the tie brick is more significant and changes the flow dynamics in  
 316 the furnace for the coupled equations. Therefore, while studying aerodynamics in the anode baking  
 317 furnace, it is important to consider the non-isothermal flow model.

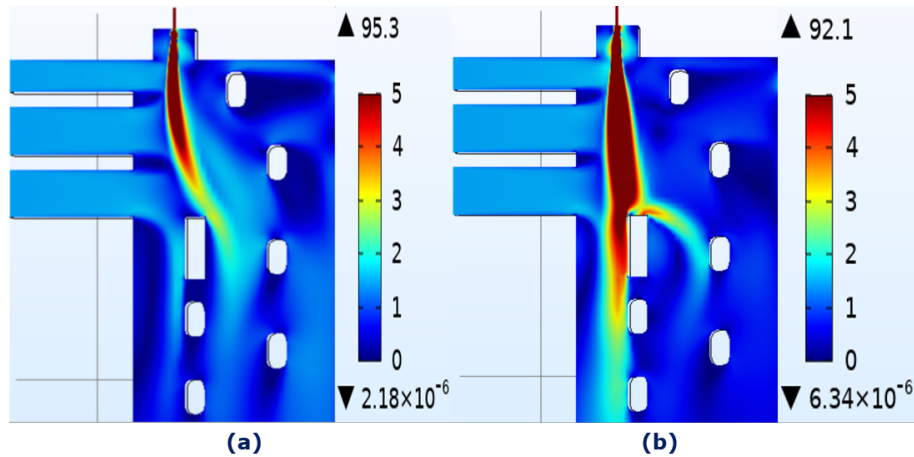


**Figure 10.** The color plots of velocity magnitude at the symmetry plane for a) uncoupled and b) coupled flow and energy equations for baseline model with Mesh 1

### 318 3.3. Comparison of Mesh 1 and Mesh 2

319 In the previous paper [10], the results with the meshing carried out by COMSOL are discussed.  
 320 Due to the physically unrealistic computation of turbulent viscosity ratio with the COMSOL mesh,  
 321 an alternate meshing tool, cfMesh, is considered for the study. After confirming the precise turbulent  
 322 viscosity ratio with this meshing tool, mesh with comparable element sizes is prepared with the default  
 323 mesher from COMSOL. The details of these meshes are discussed in section 2.3. The comparison of  
 324 velocity with the two meshing techniques, namely, by COMSOL (Mesh 2) and cfMesh (Mesh 1) is  
 325 provided in Figure 12 (a) and (b), respectively. It can be observed that the velocity magnitude from  
 326 Mesh 1 develops symmetrically as opposed to Mesh 2 in which it is bent towards left. Due to the  
 327 symmetrical development of jet in Mesh 1, the jet encounter the first tie-brick and have a stream split  
 328 towards the right. As opposed to this, the jet with Mesh 2 does not encounter the brick to a significant  
 329 extent. Therefore, most of the flow happens at the left of the first tie-brick for Mesh 2. It should be  
 330 noted that the number of elements required to obtain results with COMSOL is approximately 8 times  
 331 higher as compared to the cfMesh mesh.

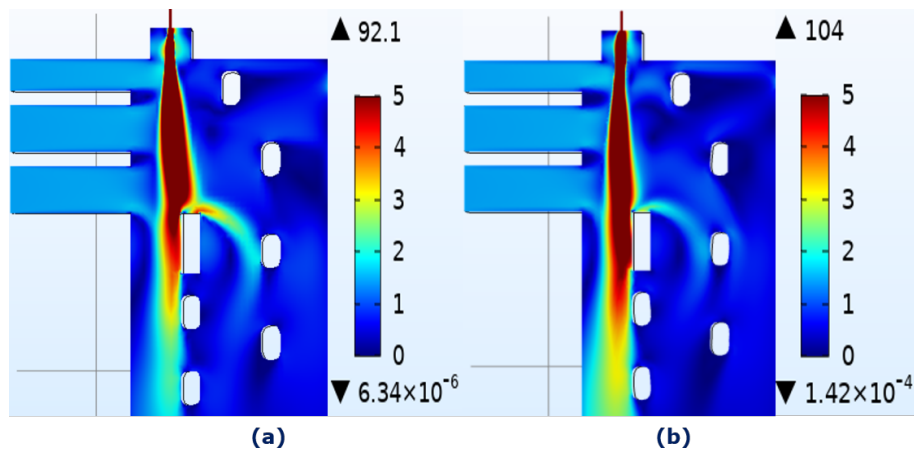


**Figure 11.** The color plots of velocity magnitude at the symmetry plane generated by a) cfMesh (Mesh 1) and b) COMSOL mesh (Mesh 2)

332 The temperature comparison for the two meshes, Mesh 1 and Mesh 2 is similar to the velocity  
 333 comparison. It follows the pattern of flow dynamics. The difference between the temperature  
 334 distribution obtained by the two meshes is again due to the way the jet encounters the first tie-brick.  
 335 This shows the strong coupling of temperature and flow dynamics based on the density.

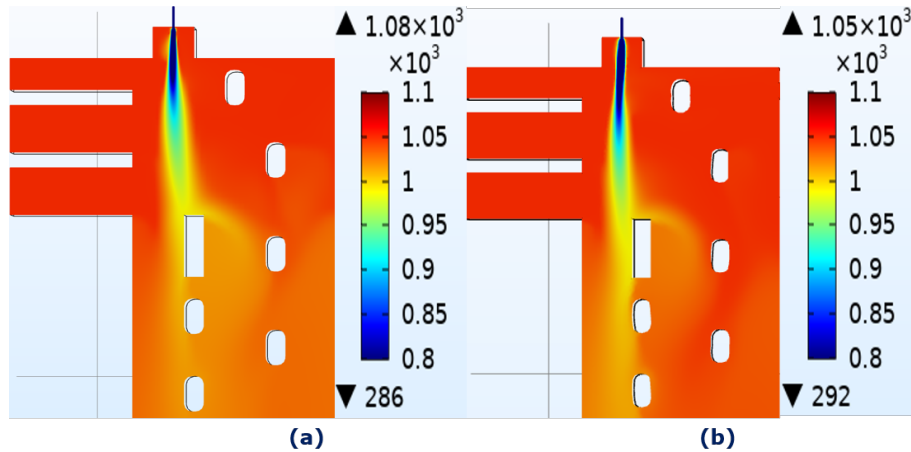


**Figure 12.** The color plots of temperature at the symmetry plane generated by a) cfMesh (Mesh 1) and b) COMSOL mesh (Mesh 2)

336 Further comparison of turbulent viscosity ratio with the two meshing techniques is as shown  
 337 in Figure 13 (a) and (b), respectively. It is important to analyze the turbulent quantities since the  
 338 combustion modeling that follows from the turbulent flow modeling depends on the turbulence  
 339 parameters. It can be observed that the turbulent viscosity ratio immediately near the fuel outlet is  
 340 lower with the COMSOL mesh as compared to the cfMesh. Moreover, the turbulent viscosity ratio  
 341 starts dissipating with the COMSOL mesh. Both these observations can be attributed to the higher  
 342 numerical diffusion with the COMSOL mesh. Due to the dissipation with the COMSOL mesh, the  
 343 flow dynamics downstream such as near the obstacle of the tie-brick are affected. Since the NO<sub>x</sub>  
 344 formation is restricted to this region, the changes in the flow dynamics are translated into the thermal  
 345 NO<sub>x</sub> formation phenomena as well.

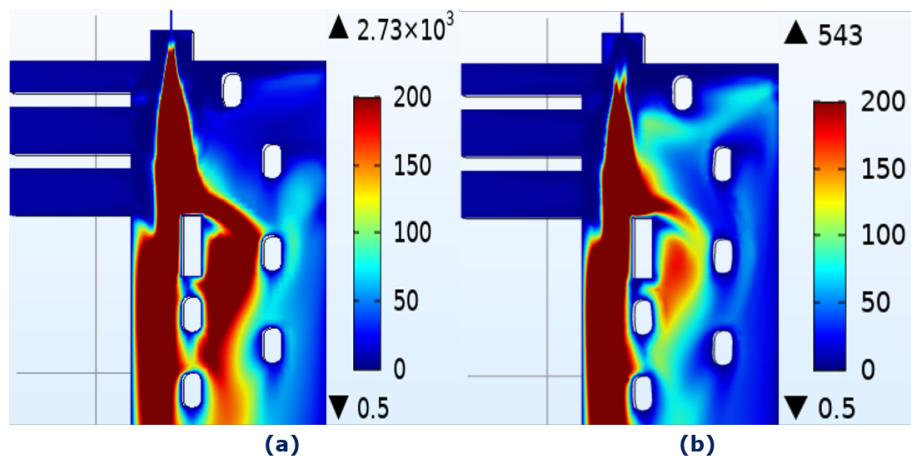


**Figure 13.** The color plots of turbulent viscosity ratio at the symmetry plane generated by a) cfMesh (Mesh 1) and b) COMSOL mesh (Mesh 2)

### 346 3.4. Comparison of Mesh 1 and Mesh 3

347 The idea of local mesh refinement in the region of interest is well known. For large models such  
 348 as the industrial furnaces, it is important to identify the region which is sensitive to the flow dynamics.  
 349 In the present study, such a region lies beneath the fuel outlet. Therefore, in this section, the sensitivity  
 350 of the results on the local refinement in the region of jet development is studied. Two meshes with  
 351 varying local refinement (Mesh 1 and Mesh 3) are generated by cfMesh software. The representation  
 352 and description of these meshes are given in the mesh section (Figure 6). The comparison of velocity  
 353 magnitude with the two meshes is as shown in Figure 14). The quick analysis suggests that the results

354 of Mesh 3 is less diffused as compared to that of Mesh 1 which is refined underneath the fuel outlet.  
 355 However, the contradiction in the results can be better explained with the help of comparison of  
 356 turbulent viscosity ratio presented in Figure 15. The effect of local refinement is prominent on the  
 357 turbulent viscosity ratio as compared to the velocity magnitude. The mesh that does not have local  
 358 refinement (Mesh 3) has a lower turbulent viscosity ratio immediately near the fuel outlet as compared  
 359 to the one with local refinement. The effect of turbulence is better captured with locally refined mesh.  
 360 The effect of better refinement underneath the jet (Mesh 1) resolves velocity magnitude in such a  
 361 way that it encounters the first obstacle without bending the jet. In case of the jet that does not have  
 362 refinement, the jet is bent towards left and does not encounter the obstacle. Therefore, the kinetic  
 363 energy for the jet with Mesh 3 is not dissipated resulting into longer jet. Therefore, the numerical  
 364 diffusion effect can not be concluded from the velocity magnitude plot. The deeper penetration of the  
 365 jet with Mesh 3 is due to the bending of the jet towards left. The comparison of turbulent viscosity  
 366 ratio provides better judgement of the diffusive behaviour of Mesh 3 as compared to Mesh 1. The  
 367 comparison of temperature with the two meshes shown in Figure 16) follows the velocity magnitude  
 368 plot. Studying such effects near the burner is important since this is the region where NO<sub>x</sub> is generated.

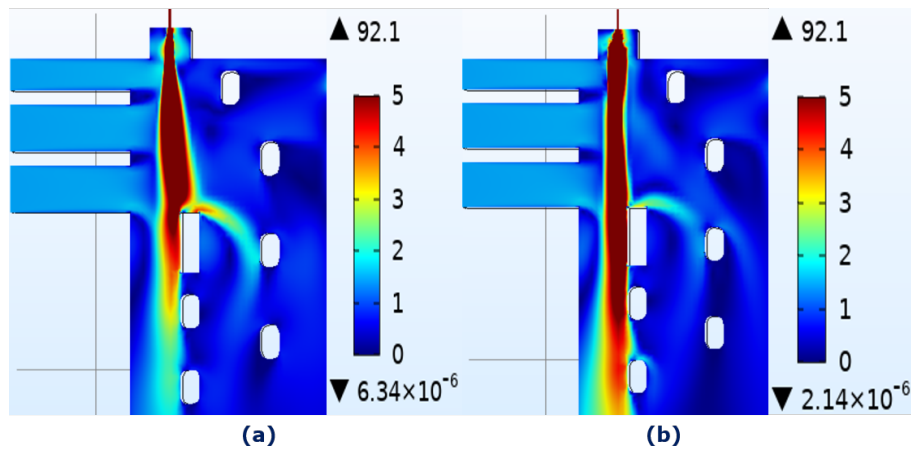


**Figure 14.** The color plots of velocity magnitude at the symmetry plane generated by cfMesh software 1) with jet refinement (Mesh 1) and b) without jet refinement (Mesh 3)

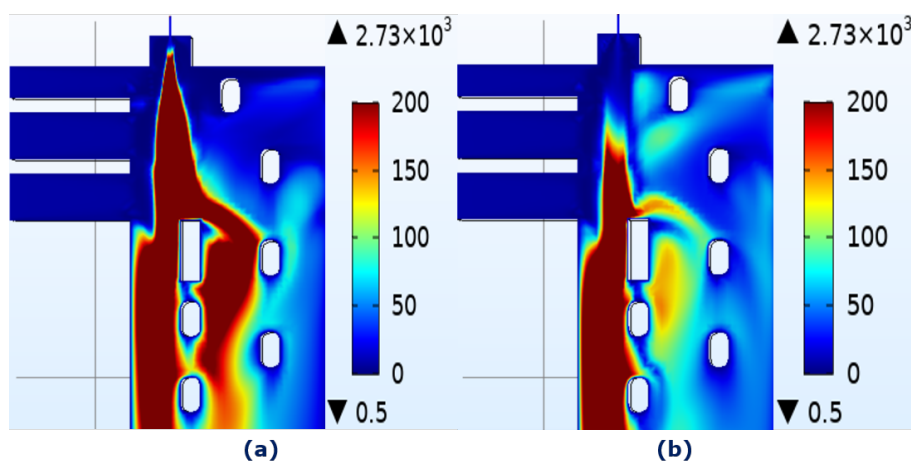


**Figure 15.** The color plots of turbulent viscosity ratio at the symmetry plane generated with the mesh of cfMesh software 1) with jet refinement (Mesh 1) and b) without jet refinement (Mesh 3)

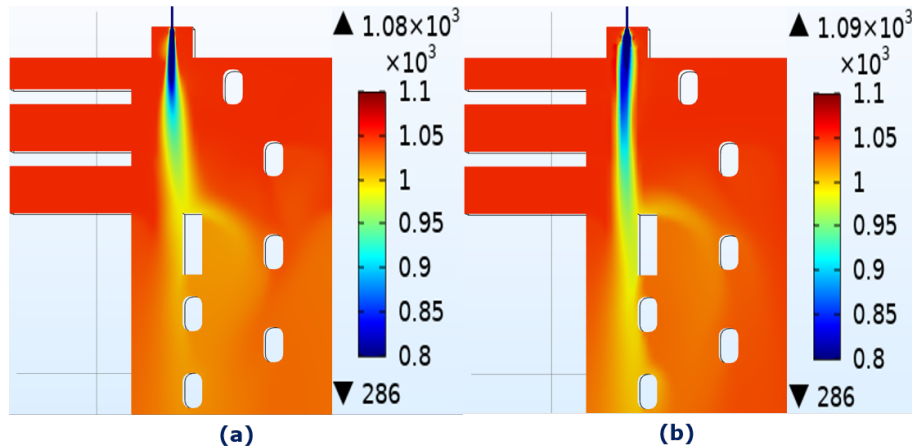


**Figure 16.** The color plots of temperature at the symmetry plane generated by cfMesh software 1) with jet refinement (Mesh 1) and b) without jet refinement (Mesh 3)

### 369 3.5. Realizable $k-\epsilon$ model

370 The realizable  $k-\epsilon$  model is the improved model of the standard  $k-\epsilon$  model in which the dependence  
 371 of mean flow distortion on turbulent dissipation is accounted for. The realizable  $k-\epsilon$  model is known to  
 372 provide well-quantified results for the round jets. The numerical diffusion introduced by the realizable  
 373  $k-\epsilon$  model is lesser than compared to the standard  $k-\epsilon$  model. However, the convergence with the  
 374 realizable  $k-\epsilon$  model is not easy to achieve for complex geometries such as anode baking furnace. The  
 375 baseline model Mesh 1 explained in the previous section fails to converge for the realizable  $k-\epsilon$  model.  
 376 In the case of the realizable  $k-\epsilon$  model, more constraints are introduced. There are several studies  
 377 carried out to analyze these constraints which would provide techniques to achieve convergence with  
 378 the realizable  $k-\epsilon$  model.

379 The discussion on the results of the standard  $k-\epsilon$  model suggests that the higher numerical  
 380 diffusion introduced by the low-quality mesh affects the results, especially the turbulent viscosity  
 381 ratio. The turbulent viscosity is of primary importance with respect to the difference of standard and  
 382 realizable  $k-\epsilon$  model. Therefore, the non-convergence of the realizable  $k-\epsilon$  model might be due to the  
 383 insufficient mesh resolution at the fuel outlet. A test case is run on the 2D model to recognize the effect  
 384 of mesh resolution in the direction perpendicular to the jet flow. The mesh with higher resolution  
 385 shows convergence whereas the model fails to converge for the mesh with lower resolution. However,  
 386 the baseline model modified by removing the fuel inlet also fails to converge. This suggests that apart  
 387 from the sufficient resolution of mesh at the fuel outlet, other regions needs to be investigated further  
 388 to achieve convergence.

389 Moreover, other factors that might be responsible for the non-convergence of the realizable  $k-\epsilon$   
 390 model are studied including the stabilization techniques. COMSOL Multiphysics applies consistent  
 391 and inconsistent stabilization techniques as described in the simulation details section. The inconsistent  
 392 stabilization technique introduces isotropic artificial diffusion to the equation. If the flow is convection  
 393 dominated i.e. for the higher Peclet number, the numerical problem may become unstable. Isotropic  
 394 diffusion in such respect may be used as a stabilization technique. The extent of the isotropic diffusion  
 395 can be controlled by the stabilization parameter which ranges from 0 to 1. The stabilization parameter,  
 396 that controls the extent of the artificial diffusion is varied and the effect on the convergence behavior is  
 397 analyzed. The addition of artificial diffusion with higher stabilization parameter aids in convergence  
 398 compensating the accuracy. As discussed in the earlier sections, the higher numerical diffusion (added  
 399 artificially in this case) impacts the turbulent viscosity ratio more than velocity and temperature.

400 The role of the solver in the non-convergence is discussed. The non-linear flow solver of COMSOL  
 401 Multiphysics is described in Figure 7. The convergence of the segregated solver is achieved when  
 402 each non-linear segregated step is converged. Furthermore, for each non-linear segregated step, a

403 damped Newton method is applied in which the solver assumes several linear steps. To understand  
404 the effect of the tolerance of the linear solver on the convergence, a test case with a simple rectangular  
405 channel is considered. The iso-thermal non-linear solver is run for various tolerances of the linear  
406 solver. However, even with the more stringent tolerance criteria such as  $10^{-14}$  of GMRES iterative  
407 linear solver, the convergence behavior is similar to more relaxed tolerance criteria of  $10^{-3}$ . This  
408 suggests that the non-convergence of the realizable  $k-\epsilon$  model is not dependent on the accuracy of the  
409 linear solver.

410 As described in the simulation details, the pseudo time stepping accelerates the convergence  
411 towards a steady-state by introducing a pseudo time step. The pseudo time step is related to the local  
412 CFL number and can be made more stringent with the PID regulator. Another test case on a simpler  
413 geometry is carried out. It is observed that as compared to the default time step, the convergence  
414 with the smaller time steps is decreasing faster. However, the progress of the CFL ratio now becomes  
415 extremely slow. This suggests that it generates better initial guesses for the Newton iteration in the  
416 next time steps. These improved initial guesses however fail to compensate for the mesh resolution.

417 The study of the realizable  $k-\epsilon$  model with detailed analysis is still in progress. It is important to  
418 obtain results of velocity, temperature, and turbulent viscosity ratio to a sufficient resolution in order  
419 to compute accurate NOx prediction.

#### 420 4. Conclusions

421 A detailed analysis of turbulent flow modeling has been carried out and it can be concluded that  
422 the turbulent quantities are more sensitive to the mesh as compared to the velocity. The non-Cartesian  
423 mesh obtained by the COMSOL default solver introduces high diffusion leading to physically incorrect  
424 computation of turbulent viscosity ratio. To obtain the Cartesian mesh, the cfMesh software is used.  
425 The workflow for generating meshes with cfMesh software and importing it into COMSOL has been  
426 developed. The two meshing techniques (the default COMSOL mesher and cfMesh meshing tool)  
427 are compared and it can be concluded that the Cartesian mesh generated by cfMesh is required for  
428 accurate computation of turbulent viscosity ratio. Furthermore, the local refinement in the region of  
429 interest, underneath the burner outlet, in this case, improves the computation of turbulent viscosity  
430 ratio. Such refinement should be employed for accurate prediction of NOx which is highly dependent  
431 on the aerodynamics. The standard  $k-\epsilon$  model is robust towards the convergence of the anode baking  
432 model even for the Cartesian refined mesh which has less numerical diffusion. The realizable  $k-\epsilon$   
433 model that accounts for a more accurate definition of turbulent viscosity needs further investigation to  
434 obtain accurate results.

#### 435 References

- 436 1. Gaba, A. and Felicia, S., Reduction of Air Pollution by Combustion Processes. *The Impact of Air Pollution on*  
437 *Health, Economy, Environment and Agricultural Sources* **2011**, 10.5772/16959.
- 438 2. Richard C. Flagan and Seinfeld, J.H., Fundamentals of air pollution engineering. *Prentice Hall* **1988**,  
439 9780133325379, <http://authors.library.caltech.edu/25069/>.
- 440 3. Baukal, C.E., Industrial Combustion Pollution and Control. *Environmental Science & Pollution* **2003**, CRC  
441 *Press*, 9780203912782.
- 442 4. Bui, R. T., Charette, A. and Bourgeois, T., Simulating the process of carbon anode baking used in the  
443 aluminum industry. *Metallurgical Transactions B* **15.3** **1984**, 487-492.
- 444 5. Grégoire, F. and Gosselin, L., Comparison of three combustion models for simulating anode baking furnaces.  
445 *Int. J. Therm. Sci.* **2018**, vol. 129, pp. 532-544.
- 446 6. Tajik, A.R., Shamim, T., Ghoniem, A.F. and Abu Al-Rub, R.K., The effects of flue-wall design modifications  
447 on combustion and flow characteristics of an aluminum anode baking furnace-CFD modeling. *Appl. Energy*  
448 **2018**, vol. 230, pp. 207-219.

- 449 7. Tajik, A.R., Shamim, T., Ghoniem, A.F. and Abu Al-Rub, R.K., CFD Modelling of NO<sub>x</sub> and Soot Formation in  
450 Aluminum Anode Baking Furnace. *ASME International Mechanical Engineering Congress and Exposition*. **2018**,  
451 Vol. 52118. *American Society of Mechanical Engineers*.
- 452 8. Besson, S., Bache, S., Bourgier, A., Schneider, J.P. and Conte, T., Modelling of Gas Injection on Anode Baking  
453 Furnace and Application to Operations. *Light Metals.Springer, Cham* **2020**, pp. 1196-1202.
- 454 9. Paniconi, C. and Putti, M., A comparison of Picard and Newton iteration in the numerical solution of  
455 multidimensional variably saturated flow problems. *Water Resources Research* **1994**, 30(12), pp.3357-3374.
- 456 10. Nakate, P., Lahaye, D., Vuik, C, Talice, M., Computational study of the anode baking industrial furnace. *Am.*  
457 *flame Res. Soc. Conf.* **2019**.
- 458 11. Juretic, F., cfMesh version 1.1 users guide [http://cfMesh.com/wp-content/uploads/2015/09/User\\_Guide-](http://cfMesh.com/wp-content/uploads/2015/09/User_Guide-cfMesh_v1.1.pdf)  
459 [cfMesh\\_v1.1.pdf](http://cfMesh.com/wp-content/uploads/2015/09/User_Guide-cfMesh_v1.1.pdf).
- 460 12. Grotjans H. and Menter F., Wall Functions for General Application CFD Codes. *ECCOMAS 98, Proceedings of*  
461 *the 4th Computational Fluid Dynamics Conference John Wiley Sons* **1998**, pp.1112-1117.
- 462 13. Hughes, T.J., Franca, L.P. and Balestra, M., A new finite element formulation for computational fluid  
463 dynamics: V. Circumventing the Babuška-Brezzi condition: A stable Petrov-Galerkin formulation of the  
464 Stokes problem accommodating equal-order interpolations. *Computer Methods in Applied Mechanics and*  
465 *Engineering* **1986**, 59(1), pp.85-99.
- 466 14. Donea, J. and Huerta, A., Finite element methods for flow problems *John Wiley Sons*.**1986**.
- 467 15. COMSOL Multiphysics version 5.4 users guide [https://doc.comsol.com/5.4/doc/com.comsol.help.cfd/](https://doc.comsol.com/5.4/doc/com.comsol.help.cfd/CFDModuleUsersGuide.pdf)  
468 [CFDModuleUsersGuide.pdf](https://doc.comsol.com/5.4/doc/com.comsol.help.cfd/CFDModuleUsersGuide.pdf).

469 © 2020 by the authors. Submitted to *Fluids* for possible open access publication under the terms and conditions  
470 of the Creative Commons Attribution (CC BY) license (<http://creativecommons.org/licenses/by/4.0/>).